# Evidence of the Electrochemical Ca²⁺ Intercalation in Anatase Nanotubes

Andrea Ceppetelli[+],[a, b] Matteo Busato[+],[b] Gabriele Dilena,[b] Carmen Cavallo,[c] Maria Assunta Navarra,[b, d] Paola D'Angelo,[b] Laura Silvestri,[f] Priscilla Reale,[g] Antonino Santoni,[g] Lorenzo Stievano,*[a, e] and Sergio Brutti*[b, d]

Here, we demonstrate the electrochemical intercalation of Ca²⁺ ions within the lattice of anatase nanotubes (a-NTs) synthesized by hydrothermal treatment of TiO₂/NaOH precursors followed by Na⁺/H⁺ ion exchange and H₂O-loss at high temperature in air. Scanning electron microscopy, X-ray diffraction, and Raman spectroscopy confirm the formation of nanosized anatase, whereas transmission electron microscopy highlights the formation of nanotubular morphologies with an average diameter of 10 nm. TiO₂ electrodes are able to deliver reversible specific capacities in aprotic batteries vs. calcium metal or in hybrid configurations vs. capacitive activated carbon using aprotic electrolytes (*i.e.*, Ca(BH₄)₂ in tetrahydrofuran or Ca(TFSI)₂ in dimethoxyethane, respectively). The electrochemical intercalation of Ca²⁺ ions into the anatase lattice is confirmed by X-ray absorption spectroscopy in close comparison with Na⁺ and Li⁺ intercalations. Ca²⁺ incorporation leads to the partial amorphization of the TiO₂ lattice despite the limited Ca/Ti ratio (*i.e.*, 0.09) obtained in discharge. The analysis of the extended X-ray absorption fine structure region allows the determination of the local structure of the incorporated Ca²⁺ ions and confirms that a disordered environment is obtained after the electrochemical reaction.

## Introduction

Innovative redox chemistries based on multivalent metals are the current most challenging research field for the demonstration of disruptive concepts in the field of electrochemical energy storage technologies.[1] Among the currently explored multivalent ion chemistries for aprotic batteries including Mg, Ca, Zn and Al, calcium emerges for the excellent balance of low redox potential, small ionic radius, abundance on Earth's crust, small costs of commodities as well as theoretical performance in line with that of Na-ion batteries.[2] On the other hand, calcium-ion batteries (CIBs) as well as all related technologies are currently at a very low level of technology readiness (TRL). In fact, their development is facing multiple challenges that are limiting their progress:[3]

(a) the very inefficient electrochemical calcium metal stripping reaction that easily leads to the precipitation of byproducts on the calcium metal surface (e.g., CaF₂, CaCO₃, CaO);[4]

(b) the lack of active materials for positive and negative electrodes able to efficiently and reversibly (de)incorporate calcium ions;[5]

(c) the lack of stable and reliable electrolytes with good transport properties able to deliver a reversible stripping/deposition of calcium with minimal degradation.[6–10]

Despite these major challenges, huge efforts have been spent worldwide by various research teams to develop reliable active materials for CIB electrodes.[2,3,5,11] Focusing on negative electrode materials, besides the highly problematic calcium metal, anodes for CIBs able to deliver a reversible performance can be grouped into three classes:[11]

I. Carbon-based anodes able to electrochemically intercalate Ca²⁺ and its solvating shell.

II. Polymeric materials able to electrochemically incorporate Ca²⁺ ions, mostly in their solvated form.

III. Metals able to incorporate calcium *via* an electrochemical alloying of Ca²⁺ ions.

Remarkably, the mechanism of reversible incorporation/de-incorporation of Li⁺/Na⁺/K⁺ ions into inorganic crystalline lattices, *e.g.*, TiO₂, MoO₂, graphite[12–16] is apparently ineffective

[a] A. Ceppetelli,[+] L. Stievano
Institut Charles Gerhardt Montpellier (ICGM), Univ. Montpellier, CNRS, ENSCM, Montpellier, France
E-mail: lorenzo.stievano@umontpellier.fr

[b] A. Ceppetelli,[+] M. Busato,[+] G. Dilena, M. A. Navarra, P. D'Angelo, S. Brutti
Dipartimento di Chimica, Università di Roma La Sapienza, Piazzale Aldo Moro 5, 00185 Roma, Italy
E-mail: sergio.brutti@uniroma1.it

[c] C. Cavallo
Centre for Materials Science and Nanotechnology (SMN), Oslo University, Sem Sælands vei 26, 0371, Oslo, Norway

[d] M. A. Navarra, S. Brutti
GISEL-Centro di Riferimento Nazionale per i Sistemi di Accumulo Elettrochimico di Energia, 50121 Firenze, Italy

[e] L. Stievano
Réseau sur le Stockage Electrochimique de l'Energie (RS2E), CNRS, Amiens, France

[f] L. Silvestri
TERIN-PSU-ABI, ENEA C.R. Casaccia, via Anguillarese 301, Rome 00123, Italy

[g] P. Reale, A. Santoni
FSN-TECFIS-MNF, ENEA, C.R: Frascati, via E. Fermi 45, Frascati 00044, Italy

[+] A. Ceppetelli and M. Busato contributed equally to this work and share the first authorship.

🖳 Supporting information for this article is available on the WWW under https://doi.org/10.1002/batt.202400183

**Batteries & Supercaps**

Research Article
doi.org/10.1002/batt.202400183

**Chemistry Europe**
European Chemical
Societies Publishing

in the case of calcium and, as far as we know, the demonstration of an electrochemical incorporation of bare $Ca^{2+}$ ions in almost unaltered ordered hosts is still missing so far in the literature, for negative electrodes.

In this work, we demonstrate the ability of nanostructured titanium oxide nanotubes to intercalate $Ca^{2+}$ ions. The reversible electrochemical activity of anatase nanotubes (a-NTs) in galvanostatic tests at room temperature is carried out either in a calcium metal half-cell or in a pseudocapacitive hybrid cell using a liquid $Ca^{2+}$ aprotic electrolyte. The experimental evidence of an electrochemical intercalation of $Ca^{2+}$ in the anatase lattice is obtained by *ex situ* Ti and Ca K-edge X-ray absorption spectroscopy (XAS). The structural modifications induced by the incorporation of calcium into the $TiO_2$ structure was analyzed by modeling the extended X-ray absorption fine structure (EXAFS) region of the XAS spectra in close comparison to analogous lithiated and sodiated anatase samples.

## Experimental Methods

### Synthesis of the Anatase Nanotubes

a-NTs were synthesized by optimized alkaline hydrothermal route.[17] Bulk Titania ($TiO_2$ powder, Sigma Aldrich) was dispersed in 10 M NaOH (98%, Sigma Aldrich) solution (Ti:Na = 1:13 w/w) with a series of stirring and sonication steps followed by heating at 150°C for 2 hours in a Teflon-lined autoclave. The hydrothermal treatment is known to produce sodium-titanate nanosheets that roll-up and form nanotubes in solution.[17] After this process, the product is filtered and washed to remove the excess of NaOH. The product obtained at this stage of the process consists of hydrated Na-titanate nanotubes, $Na_yH_{1-y}Ti_nO_{2n-1}$, which were ion exchanged, using a 0.01 M aqueous solution of hydrochloric acid added dropwise under continuous stirring until pH = 4 was reached to obtain the de-sodiated $H_2Ti_3O_7$. In order to confirm and describe the evolution of morphology and composition of the sodiated NTs upon acidification, four samples at different stages of the ion-exchange were collected and investigated with field-emission scanning electron microscopy (FESEM, see below for technical details) and EDX (energy-dispersive X-rays Bruker probe). The final product was filtered, washed with a minimal amount of water, and dried overnight at 80°C under vacuum. The sample was annealed at 380°C for 5 minutes with a heating rate of 0.4°C/min.

### Physico-Chemical Characterization

FESEM coupled with EDX experiments were carried out at the CNIS Center for Nanotechnology and Innovation of Sapienza by employing an Auriga Zeiss electron microscope. Wide-angle X-ray powder diffraction (XRD) patterns were collected by using either a Philips X'PERT or a Bruker Advance D8 diffractometer, both equipped with a Cu Kα source, λ = 1.5418 Å using in all cases an angular scan in the range of 10°–100° with a step size of 0.02°. MicroRaman spectroscopy experiments were carried out using a Dilor Raman system equipped with an He—Ne (632.7 nm) laser source, a Semrock RazorEdge® ultrasteep long-pass edge filter and a Peltier cooled CCD detector. Transmission electron microscopy (TEM) analysis was carried out using a FEI Tecnai cryo-TEM instrument: samples were prepared by evaporating a drop of an ethanol suspension of anatase NTs onto a holey carbon Cu mesh grid.

### Cells Assembly and Electrochemical Tests

Electrode composite films were prepared by tape-casting on Cu foil (0.1 mm, Sigma Aldrich). The composite slurry was obtained by mixing a-NTs with a conductive carbon additive (Super P, Alfa Aesar) and polyvinylidene fluoride (PVdF, Solef® 5130) as the binder with a mass ratio of 70/20/10, respectively, in $^{18}$N-methyl-2-pyrrolidone (NMP, Sigma Alrich). The casted film was dried in air before punching out circular electrodes (diameter 9 mm), which were then further dried *in vacuo* at 90°C overnight. a-NTs composite electrodes were also prepared on Al foil (18 μm, Good-Fellow) following the same procedure to minimize the current collector corrosion in the aprotic electrolyte.[18] Pelletized a-NTs electrodes were manufactured starting from the same composite mixture by using a hydraulic-press at room temperature and a Specac 13 mm die set at 5 tons cm$^{-2}$. Free standing capacitive electrodes were made using activated carbon (AC, YP-50F, Kuraray) and polytetrafluoroethylene dispersion (PTFE 60 wt% in water, Sigma Aldrich), used as received. The mass ratio of AC active material and PTFE binder was 95/5. Calcium metal (ACI Alloys, Inc) electrodes were obtained starting from calcium foils rolled using a calendaring machine (MTI corp.) to an approximate thickness of 100 μm: the surface of the Ca foils was scratched in the glove box to remove the passivating layer and punched into disks (diameter 9 mm). Lithium (Li, 99.9%, Sigma Aldrich) and sodium (Na, 99.8% Sigma Aldrich) electrodes were punched (diameter 9 mm) from thin foils and pressed onto a stainless-steel current collector.

Electrolytes for calcium-based cells were formulated and prepared starting from solvents dried under molecular sieves and calcium salts in an Iteco Eng SGS30 Ar-glove box with a moisture content below 1 ppm. Molecular sieves (3 Å, Alfa Aesar) were preliminarily dried at 300°C for 24 h in a Muffle Furnace (Nabertherm up to 1100°C). Tetrahydrofuran (THF, Sigma Aldrich, 99.9%), 1,2-dimethyl-glycol ether (DME, Sigma Aldrich, 99.5%) were dried over the pre-dried molecular sieves for one week. Calcium bis(trifluoromethanesulfonyl imide (Ca(TFSI)$_2$, Solvionic, 99.5%) was dried at 100°C under vacuum before use, whereas calcium borohydride (Ca(BH$_4$)$_2$, Sigma Aldrich) was used as received. Calcium-based electrolytes were prepared by dissolving the appropriate amount of Ca(TFSI)$_2$ in DME to obtain a molality of 0.5 mol/kg for the pseudo capacitive cell tests, and by dissolving Ca(BH$_4$)$_2$ in THF to obtain a molality of 1 mol/kg for the electrochemical tests in Ca metal half-cells. The aprotic electrolyte for lithium cells was a commercial formulation from Merck (*i.e.*, LP30, 1 mol/l solution of lithium hexafluorophosphate (LiPF$_6$) in an ethylene carbonate (EC) - dimethyl carbonate (DMC) 1:1 vol. solvent mixture). The aprotic electrolyte for the sodium cell was prepared by dissolving 1 mol of NaClO$_4$ (Alfa Aesar) per liter of EC-propylene carbonate (PC) 1:1 vol solvent mixture (Sigma Aldrich).

In all cases, Whatman glass fiber disks (thickness 1.55 mm) soaked with 0.1 ml of electrolyte were used as the separators. The assembly of cells (a-NTs/electrolyte/CE) and all the manipulations were carried out inside Ar-filled glove boxes (O$_2$ and H$_2$O < 1 ppm). The testing cells for the electrochemical experiments were made by assembling a-NTs/electrolyte/Ca, Li, or Na using ECC-STD cells, and a-NTs/electrolyte/AC, Ca as reference electrodes using ECC-Ref commercial cells from EL-Cell. Electrochemical tests were carried out using an MTI battery testing system or an IVIUM Vertex electrochemical testing station. Current rates were calculated with respect to the mass of the active material in the electrodes.

### XAS Measurements and Data Analysis

XAS experiments were carried out at the XAFS beamline of ELETTRA Synchrotron[19] on pristine materials and *post mortem* electrodes.

**Batteries & Supercaps**

Research Article
doi.org/10.1002/batt.202400183

**Chemistry Europe**
European Chemical
Societies Publishing

After cycling, the electrochemical cells were disassembled in an Ar-filled glove box to recover the *post mortem* electrodes, which were carefully washed three times in THF and dried *in vacuo* at room temperature for 30 minutes. For the sake of comparison, similar experiments were carried out on cells *vs.* calcium, sodium and lithium to follow the electrochemical incorporation of the corresponding cations in the electrodes. Pristine samples were prepared by carefully grinding the powder in an agate mortar inside an Ar-filled glove box with boron nitride as dispersing agent to produce pellets with the optimal thickness and mass loading of the atomic species under study, *i.e.*, Ca and Ti. All samples were sealed between two Kapton windows to avoid direct contact with ambient air and loaded into a multi-sample holder operating in high vacuum conditions. Ti K-edge and, when relevant, Ca K-edge XAS measurements were carried out in transmission geometry with a Si(111) double crystal monochromator, while the storage ring was operating at 2 GeV with a beam current of 200 mA. All spectra were collected with the same experimental set-up, allowing for direct comparison among the peak intensities. Energy calibration was carried out using as reference standards $CaCO_3$ for the Ca K-edge and a titanium metal foil for the Ti K-edge. No relevant drifts or shifts of the photon energy were observed during the experiments. The Ca K-edge XAS spectrum of a 0.1 M $CaCl_2$ aqueous solution (slightly acidic) was measured as a reference. The experimental setup for this sample can be found in Ref.[20] At least two spectra were recorded and averaged for each sample. For the comparison of the X-ray absorption near edge structure (XANES) data, a linear background was fit to the pre-edge region and then subtracted from the entire spectrum, while the jump was normalized to unity with the post-edge asymptotic value chosen where the XAS oscillations are small enough to be negligible. The number of $Ca^{2+}$ ions trapped into the a-NT anode per formula unit of $TiO_2$ was derived by the corresponding jump of the spectra collected at the Ca and Ti K-edge on *post mortem* samples.

The EXAFS portion of the Ca K-edge XAS spectrum collected on the $Ca^{2+}$-intercalated a-NTs was analysed with the GNXAS code.[21,22] Amplitudes and phase shifts were calculated from clusters with fixed geometry within the muffin-tin (MT) approximation with MT radii of 0.90 Å for oxygen and 1.35 Å for calcium and titanium, as previously reported.[20] Advanced models for the exchange-correlation self-energy in the framework of the Hedin-Lundqvist scheme were used to take into account the photoelectron inelastic losses in the final state.[23] In the GNXAS approach, theoretical signals associated with *n*-body distribution functions are calculated following the multiple-scattering (MS) theory and summed to reconstruct the total theoretical contribution. A theoretical Ca–O single scattering (SS) signal was calculated to account for the first shell oxygen atoms, while the Ca–Ti contribution accounting for the second shell Ti atoms did not improve substantially the fit quality (*vide infra*). The two-body distributions are modeled as $\Gamma$-like functions depending on four structural parameters, namely the coordination number *N*, the average distance *R*, the Debye-Waller factor $\sigma^2$, and the asymmetry index $\beta$, which were optimized during the fitting procedure to obtain the best agreement with the experimental data. Note that in disordered systems, where large asymmetries in the pair distributions are observed, the average distance is no longer the maximum one, while these values coincide for symmetric Gaussian distributions ($\beta = 0$).[20,24,25] Least-squares minimizations were carried out directly on the raw data, without preliminary background subtraction or Fourier filtering. Additional non-structural parameters such as the edge ionization energy $E_0$, the amplitude reduction factor $S_0^2$, and the energy position and amplitude of the $KM_1$ double-electron excitation channel, modeled with an arctangent function, were also optimized during the fitting procedure.

## Results

### Preliminary Anatase Nanotubes Characterization

a-NTs were synthesized following a well-established hydrothermal route forming as intermediate product sodiated tri-titania nanotubes, *i.e.*, $Na_2Ti_3O_7$, which are converted into $H_2Ti_3O_7$ by $Na^+/H^+$ ion-exchange with HCl.[17] In order to monitor the evolution/preservation of the morphology of the NTs during ion-exchange, four samples at different stages were collected at various pH values and investigated by FESEM-EDX as shown in Figure 1. As expected, the titration by 0.01 M aqueous HCl is able to ion-exchange the $Na^+$ ions from the $Na_2Ti_3O_7$ lattice with $H^+$. At the end of the acidic washing, the residual Na/Ti atomic ratio is approximately 0.03, in line with the almost complete removal of $Na^+$ ions from the structure. This compositional change occurs without major alterations in the nano-morphology of the sample that preserves the nano-tubular shape in the primary particles and morphological homogeneity across the sample (cf. Figure 1).

After the ion-exchange procedure, the $H_2Ti_3O_7$ precursor was annealed in air at 380 °C to remove the structural water and promote the nano-crystallization of the Anatase NTs.[17] This
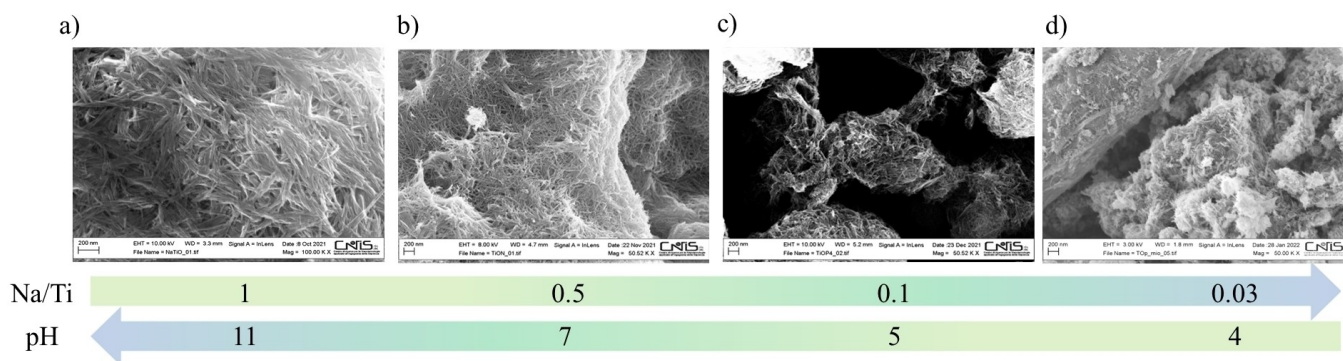


| | a) | b) | c) | d) |
|---|---|---|---|---|
| Na/Ti | 1 | 0.5 | 0.1 | 0.03 |
| pH | 11 | 7 | 5 | 4 |

**Figure 1.** Morphological evolution of the hydrated NTs at various stages of the $Na^+/H^+$ ion-exchange process. The $Na_2Ti_3O_7$ phase obtained by hydrothermal reaction has been titrated with 0.01 m aqueous HCl and the intermediate samples have been collected by filtration at different pH values and were dried at 80 °C overnight in air. The Na/Ti atomic ratio has been derived from EDX data.

high-temperature annealing preserves the nanotubular morphology of the samples as shown by the TEM micrograph in Figure 2. The de-hydrated nanotubes show a mean outer diameter of approximately 10 nm, an inner diameter of about

5–7 nm and a length ranging between 100 and 300 nm, in line with the literature.[17]

The nature of the NTs after annealing at 380 °C was checked by Raman spectroscopy and XRD (Figures 3a-b), which confirm
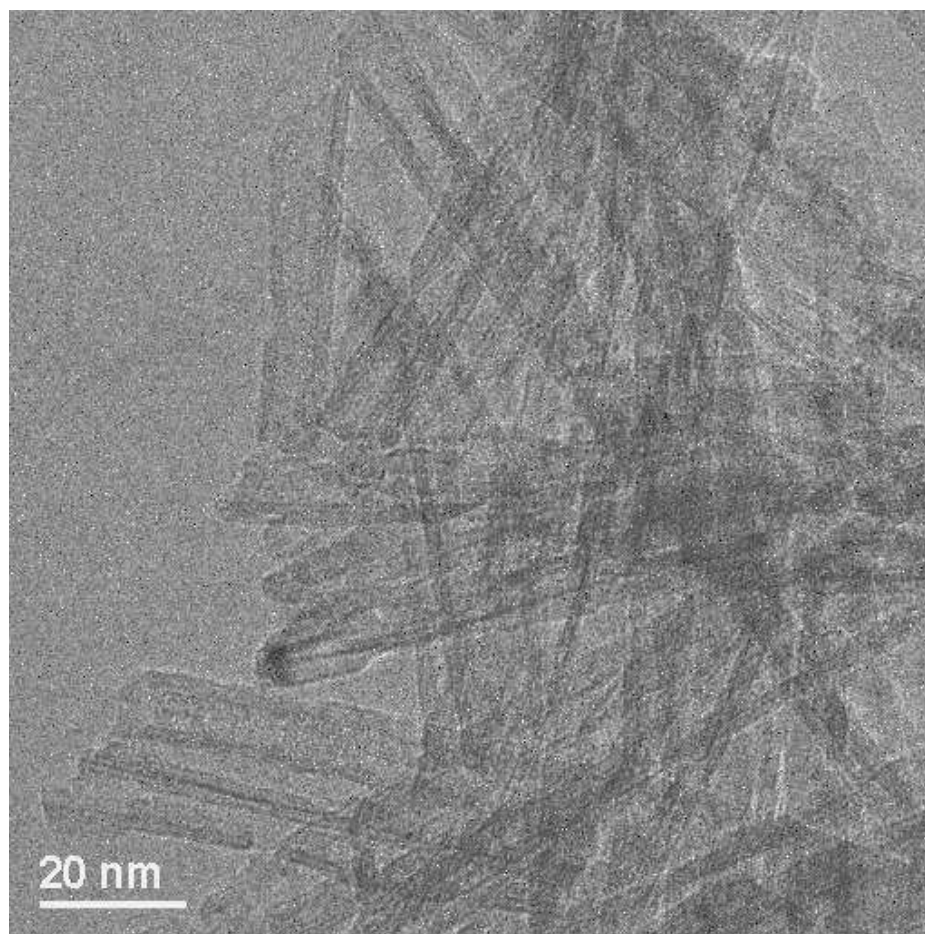


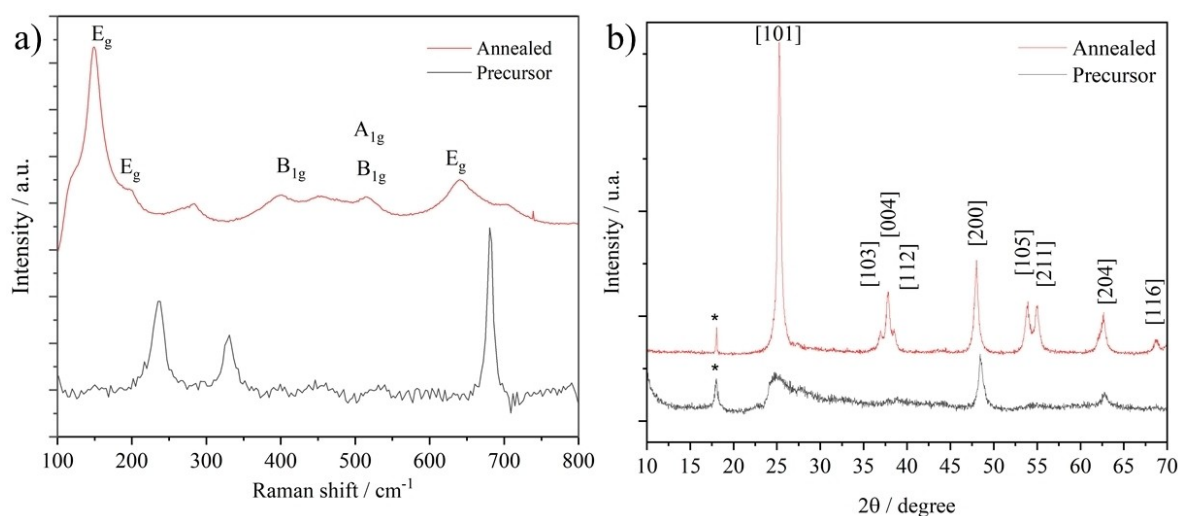**Figure 2.** TEM micrograph of the a-NTs after annealing at 380 °C.



**Figure 3.** (a) Raman spectra and (b) XRD patterns of the $H_2Ti_3O_7$ precursor and the $TiO_2$ NTs after annealing. The vibrational modes and the Bragg lines are indexed by the $TiO_2$ anatase lattice (space group I41/amd). *These peaks are due to the sample holder.

**Batteries & Supercaps**

Research Article
doi.org/10.1002/batt.202400183

**Chemistry Europe**
European Chemical
Societies Publishing

the structural rearrangement to well-crystallized anatase, indexed within the expected tetragonal systems (space group I41/amd).[17] All Raman bands of the annealed sample can be assigned to anatase phase:[26–32] the three Raman bands at 639, 197, and 149 cm$^{-1}$ are assigned to the $E_g$ modes,[26,33] while those at 280 and 698 cm$^{-1}$ suggest the formation of a tubular structure[32] and the strong peak at 149 cm$^{-1}$ is the fingerprint of the active mode of Ti–O–Ti bonds of anatase[26,32] as well as the 449 cm$^{-1}$ band.[34] The band at 515 cm$^{-1}$ corresponds respectively to the $A_{1g}$ and $B_{1g}$ modes of Ti–O bonds[26] whereas the 399 cm$^{-1}$ band can be assigned to the $B_{1g}$ modes.[26]

The structural evolution into a nanosized anatase lattice in the post-annealing NTs is also confirmed by XRD (Figure 3b). The evolution of the XRD pattern from the precursor to the annealed sample follows the expected trend[35] and discloses an expected increase in crystallinity. While the precursor shows the typical feature of a poorly crystalline hydrated titania,[17] the XRD pattern of the annealed samples reveals the presence of characteristics peaks at $2\theta = 25.6$, 36.9, 37.8, 38.5, 48.0, 53.9, 55.0, 62.0 and 68.0° corresponding to the expected reflections of the (101), (103), (004) (112) (200) 105), (211) (204) and (116) lattice planes of anatase, respectively.[27,36–38]

## Electrochemical Performance

The electrochemical activity of the anatase NTs in secondary calcium-based batteries was tested using two remarkably different cell configurations:

C1. (+) Anatase NTs-based composite electrode/Ca(BH$_4$)$_2$ 1 mol kg$^{-1}$ THF/Calcium metal (−)

C2. (+) Anatase NTs-based composite electrode/Ca(TFSI)$_2$ 0.5 mol kg$^{-1}$ DME/Activated carbon capacitive composite electrode (−) with a Ca metal reference electrode

These configurations have advantages and disadvantages. C1 is a typical half-cell configuration whereas C2 is a hybrid faradic-capacitive cell configuration. In the C1 configuration, the electrolyte consisted of a 1 mol kg$^{-1}$ solution of Ca(BH$_4$)$_2$ dissolved in THF. This electrolyte enables a partially reversible plating and stripping of Ca$^{2+}$ ions onto/from a calcium metal foil at room temperature with low polarization.[39,40] However, it

has a very narrow electrochemical stability window[40,41] restricting the electrochemical tests *vs.* Ca metal in the potential window between 0.01 and 1.8 V vs. Ca$^{2+}$/Ca. Unfortunately, up to now, a satisfactory aprotic electrolyte capable of delivering a fully reversible Ca$^{2+}$ ion deposition/stripping from the calcium metal surface is still an elusive task,[42] since strongly insulating passivation products easily precipitate at the Ca/electrolyte interphase thus easily preventing any electrochemical reaction.[43] The performance recorded for a-NT composite electrodes in a C1 cell configuration is shown in Figure 4a.

In the C1 half-cell configuration, discharge capacities ranging between 110–220 mAhg$^{-1}$ are observed for the anatase NTs electrodes, whereas much smaller values of 60–80 mAhg$^{-1}$ are recorded upon charge. These data suggest the possible electrochemical reversible intercalation/deintercalation of about 0.09–0.12 eq of Ca$^{2+}$ in the TiO$_2$ lattice. On the other hand, our data highlight a rather poor coulombic efficiency that even in the best case never exceeds 54%, suggesting the occurrence of remarkable irreversible and/or parasitic phenomena.

The average cell voltage in the C1 half cells is apparently 0.92-0.93 V vs. Ca$^{2+}$/Ca. This value is below the redox potential of the Ti$^{4+}$/Ti$^{3+}$ redox couple of the corresponding Li$^+$ (de)intercalation in the anatase lattice.[17] By considering that C1 is a two-electrode configuration, the observed average working potential can be strongly biased (*i.e.*, underestimated) by the possible occurrence of uncontrolled overpotentials at the negative counter-electrodes where the kinetically hindered electrochemical Ca-plating/stripping occurs.

To adequately estimate the working electrode potential of anatase electrodes, we also performed electrochemical tests in the C2 configuration (also implying the use of a calcium metal reference electrode) and the results are shown in Figure 4b.

In contrast to C1 configuration, a pseudo-plateau below 1.4 V in the discharge curve and above 1.8 V upon charge is observed. The reversible specific capacities measured in the C2 cells are, nevertheless, in remarkable agreement with those of the C1 one, ranging from 60 to 75 mAhg$^{-1}$ (fairly below the theoretical capacity of 355 mAhg$^{-1}$ calculated by considering the Ti$^{4+}$/Ti$^{3+}$ redox couple) with a coulombic efficiency smaller than 59%.



a) Anatase NTs | Ca(BH$_4$)$_2$ 1m in THF |Ca

J=5mA/g

b) Anatase NTs | Ca(TFSI)$_2$ 0.5m in DME | AC, Ca as reference electrodes
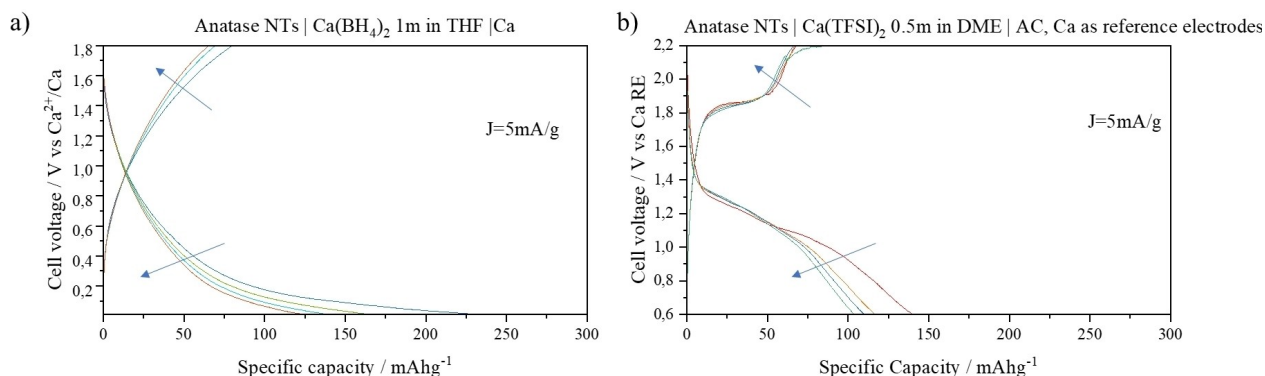
J=5mA/g

**Figure 4.** Performance of the a- NTs electrodes by using the C1 or C2 cell configurations. Current rate 5 mAg$^{-1}$; shown cycles are 2–5 of the whole galvanostatic test and are obtained after 1 activation cycle.

**Batteries & Supercaps**

Research Article
doi.org/10.1002/batt.202400183

**Chemistry Europe**
European Chemical
Societies Publishing

The most remarkable difference between the experimental results obtained for the a-NTs electrodes in C1 and C2 cell configurations is the average working potential. In fact, in the case of the hybrid configuration with the reference electrode, the mean working potential for the $Ti^{4+}/Ti^{3+}$ redox couple in the anatase lattice while intercalating $Ca^{2+}$ ions can be estimated at approximately 1.6 V $vs.$ $Ca^{2+}/Ca$, a remarkably larger value than that obtained from the two-electrode C1 configuration. As already mentioned, however, the working potential measured in the C1 configuration likely underestimates the actual value due to the overpotentials of the redox reaction at the calcium metal counter-electrode. Furthermore, a $E°$ value of 1.6 V $vs.$ $Ca^{2+}/Ca$ for calcium intercalation in anatase NTs nicely matches the working potential of the electrochemical intercalation of $Li^+$ ions in the same bulk phase.[17]

Overall, despite the technical complexity of the electrochemical tests on the a-NTs electrodes, our results suggest that the anatase lattice can reversibly accommodate approximately 0.1 eq. $Ca^{2+}$ ions in its lattice at a working potential of approximately 1.6 V $vs.$ $Ca^{2+}/Ca$.

### Post Mortem Analysis by ex situ XANES

The possible intercalation of $Ca^{2+}$ into the anatase lattice was studied by Ca and Ti K-edge XAS on *post mortem* electrodes collected from calcium-metal half-cells in the C1 configuration submitted to a controlled discharge process. Among the numerous analytical methods employed to detect variations in local structure and oxidation state, in fact, XAS stands out as an ideal technique to study disordered or poorly crystalline systems.[24,25] The versatility of XAS in simultaneously recording information on different elements was therefore exploited to study the local structure of both Ca and Ti centres, thus disclosing data from both perspectives. To carry out such dual-

edge XAS experiments, self-supported pelletized electrodes are mandatory, in consideration of the rather different concentrations of Ca and Ti. The performance of a-NT pelletized electrodes in metallic half-cells is shown in Figures 5 for Na, Li, and Ca-metal half-cells. Note that the cathodic voltage cutoff for a reversible incorporation of lithium ions in any $TiO_2$ polymorph is 1 V $vs.$ $Li^+/Li$: at lower values, lithiated $TiO_2$ is irreversibly converted into other phases.[44] Owing to this, and differently from the cases of $Na^+$ and $Ca^{2+}$ intercalation, the electrochemical reduction of a-NTs $vs.$ lithium was limited at potentials above 1 V $vs.$ $Li^+/Li$.

As expected, the increase in mass loading of the electrodes while shifting from casted films (AM = 1 mg cm$^{-2}$) to pellets (AM = 20 mg cm$^{-2}$), slightly decreases the performance for both lithium[17] and sodium[45] intercalation with respect to the literature, as well as calcium in comparison to the data shown in Figure 4. Despite this, the reduction proceeded for all samples to a reasonable extent, confirming the reliability of the experimental approach. Overall, a nominal incorporation of 0.69, 0.98, and 0.11 eq. of $Li^+$, $Na^+$, and $Ca^{2+}$ per $TiO_2$ formula unit was obtained, respectively.

Figure 6a shows the Ti K-edge normalized XANES spectra collected on pristine a-NTs and after full electrochemical intercalation of the $Li^+$, $Na^+$, and $Ca^{2+}$ ions. All the XANES spectra show the typical profile of anatase with four distinct features in the pre-edge region, labeled A1, A2, A3, and B (inset of Figure 6a), an edge shoulder identified as C, plus two edge peaks labeled as D and E.[46–48] While the latter features derive from the allowed *1s → 4p* main dipole electronic transition, the less intense pre-edge features originate from the forbidden *1s → 3d* transitions made possible by the *p-d* orbital mixing induced by the lowering of the local symmetry of the $TiO_6$ octahedra.[49,50] In the case of $TiO_2$, these transitions are caused by the mixture of dipole and quadrupole excitations connecting the Ti *1s* orbital with *3d–4p-4s* hybridized states involving not
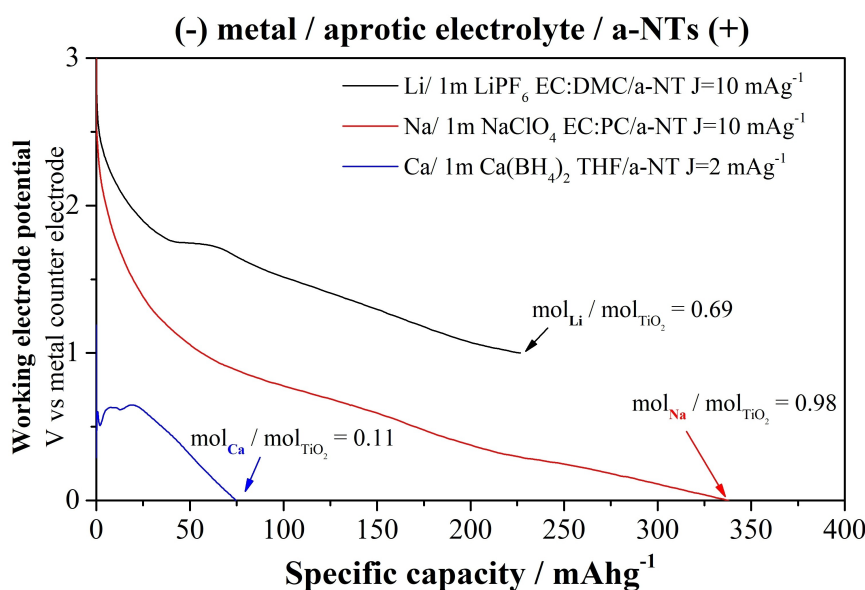


**Figure 5.** Performance of the a-NT pelletized electrodes in Li, Na, and Ca metal half-cell.
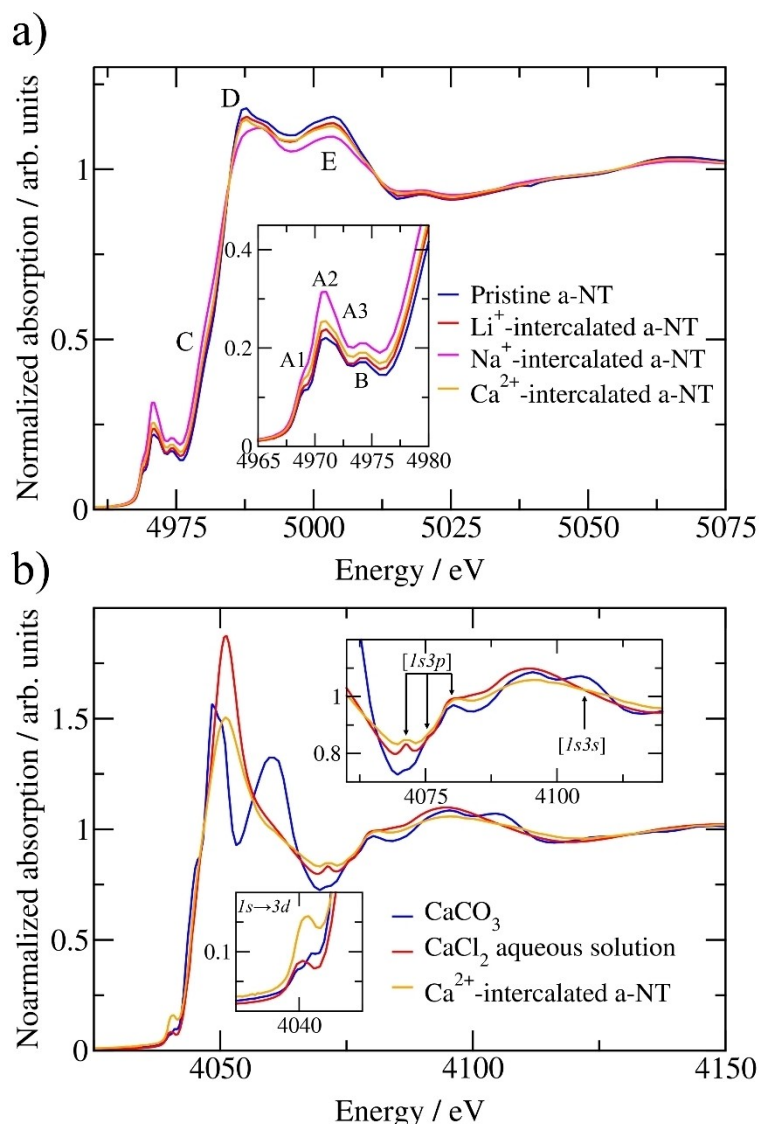
**Figure 6.** Normalized experimental XANES spectra (a) at the Ti K-edge, collected on pristine a-NTs and after full electrochemical intercalation of the Li$^+$, Na$^+$, and Ca$^{2+}$ ions; (b) at the Ca K-edge, collected on the CaCO$_3$ standard, on a 0.1 M CaCl$_2$ aqueous solution,[20] and on a-NTs after full electrochemical Ca$^{2+}$ intercalation. In the inset of Figure 6a the pre-edge peak region showing the A1, A2, A3, and B transitions is magnified. The upper inset of Figure 6b shows the energy region with the [1s3p] and [1s3s] double-electron excitation channels, while the lower inset shows the pre-edge peak region corresponding to the 1s→3d transition.

only the absorbing center but also the second shell Ti atoms, plus hybridization with the *2p* orbitals of the neighboring oxygen ligands. The assignment of the pre-edge transitions has been the center of a long-standing (and still ongoing) debate, in particular concerning the origin of the A2 peak, since this contribution is often more susceptible to modifications upon variation of the Ti local environment.[46–48,50–53] Nevertheless, a consensus has somehow been reached about the relationship between the A2 contribution and the degree of crystallinity in the TiO$_2$ lattice.[46,48,50,54,55] This conclusion derives from the empirical observation that the height of the A2 peak is enhanced in the presence of distorted or defective Ti local environments (four- or five- instead of six-fold coordination) as well as for nanostructured materials. The latter finding can be correlated with a higher fraction of undercoordinated Ti centers

at the surface of the nanoparticles compared to bulk anatase.[48,55] This is the case of the pristine a-NTs studied here, which show an intense A2 transition (inset of Figure 6a) accompanied by a shoulder at higher energies representing the A3 contribution. In contrast, the A2 transition is much less intense in the XANES spectrum of bulk anatase (Figure S1), where it only appears as a shoulder on the low-energy side of the A3 pre-peak. On the other hand, the A2 contribution is even more intense in the XANES spectrum on a TiO$_2$(B)-based amorphous phase (Figure S1). Furthermore, the amorphous phase shows a broadening of the D and E features in the so-called white-line region, which was previously connected to the increasing amorphization of the TiO$_2$ lattice.[48,51,54,56]

The XANES data collected on the a-NTs electrodes after the electrochemical intercalation of Li$^+$, Na$^+$, and Ca$^{2+}$ ions (Fig-

**Batteries & Supercaps**

Research Article
doi.org/10.1002/batt.202400183

**Chemistry Europe**
European Chemical
Societies Publishing

ure 6a) show an intensity enhancement of all the four pre-edge transitions with respect to pristine a-NTs. This result was already observed for lithium[57–60] and sodium[54,55,61,62] uptake by anatase-based materials and connected with loss of crystallinity in the $TiO_2$ matrix caused by the electrochemical reaction. It is worth noting that, in the $Ca^{2+}$-intercalated a-NTs, the intensity of the four pre-edge peaks, and in particular of the A2 feature, is higher than in the lithiated sample, but lower than in the sodiated one. This evidence suggests that the $Ca^{2+}$ intercalation introduces a degree of configurational disorder in the $TiO_2$ lattice that is comprised between those of $Li^+$ and $Na^+$ intercalation, despite the much lower nominal loading of $Ca^{2+}$ eq. per unit formula compared to $Li^+$ and $Na^+$ (vide supra). This trend is confirmed by the smoothing effect in the white-line region, following the same $Li^+ < Ca^{2+} < Na^+$ order. This result is perfectly reasonable if one considers the ionic radii of the three ions and in particular the smaller size of the $Li^+$ ion,[63] while the sodiation process in $TiO_2$-based anodes was previously observed to introduce severe structural modifications with a considerable degree of irreversibility.[54,55,61,62] In particular, $Na^+$ intercalation in anatase electrodes based on nanoparticles, where the ion uptake is expected to be more efficient, induces the loss of the typical anatase spectral profile. In the anatase $TiO_2$ lattice, the octahedral interstitial site has a radius of 0.52 Å. All three ions have larger ionic radii (0.76, 1, and 1.02 Å for $Li^+$, $Ca^{2+}$, and $Na^+$ respectively)[62] and therefore each of them induces distortions when inserting in the anatase structure. Since the ionic radii are $Li^+ < Ca^{2+} < Na^+$ this trend is followed also with respect to the structural distortion, with a significant increasing local distortion for the intercalation passing from $Li^+$ and $Ca^{2+}$ to $Na^+$. The characteristic four pre-edge peaks are indeed a fingerprint of the anatase polymorph due to the local $D_{2d}$ symmetry of the Ti centers, corresponding to a slightly distorted octahedron with two oxide ions in the apical positions with longer bond distances to Ti compared to the equatorial ones.[50] The splitting of the two A2 and A3 bands therefore mirrors a different degree of hybridization due to this distortion, while rutile generally shows only three pre-edge peaks due to its centro-symmetric $D_{2h}$ Ti site.[46,47] Although the relative intensity of the pre-edge transitions in the $Ca^{2+}$-intercalated a-NTs is altered with respect to the pristine a-NTs (Figure 6a), the four peak fingerprint is preserved, thus suggesting that the anatase shape is substantially maintained in the electrode material even after the $Ca^{2+}$ incorporation.

In Figure 6b, the Ca K-edge XANES spectrum of $Ca^{2+}$-intercalated a-NTs is compared with those of the $CaCO_3$ standard and of a 0.1 M $CaCl_2$ aqueous solution. The spectral profile of $Ca^{2+}$-intercalated a-NTs shows the presence of a small peak and two humps comprised between 25–35 eV above the edge, plus an additional bump at higher energy (inset of Figure 6b). The origin of these features was previously identified with the [1s3p] and [1s3s] double-electron excitation channels, respectively, the former one appearing as a large multiplet spread in the experimental data due to mixed configurations.[22] At first glance, the XANES spectrum of the a-NTs is similar to that of the $CaCl_2$ aqueous solution, both being considerably different from that of $CaCO_3$. In aqueous solution the $Ca^{2+}$ ion

is coordinated by eight water molecules interacting via the oxygen atom to form a relatively disordered hydration complex.[20,64] The higher similarity with a disordered-like liquid system as compared to the $CaCO_3$ standard suggests the presence of a quite disordered environment around the $Ca^{2+}$ ions intercalated in the $TiO_2$ lattice. This observation is also supported by the pre-edge peak corresponding to the $1s \rightarrow 3d$ transition (inset of Figure 6b). As already pointed out for the Ti K-edge spectra, this transition is forbidden but relaxation of the selection rule is made possible by the broken inversion symmetry introduced by the configurational disorder. The presence of a highly disordered coordination around the $Ca^{2+}$ ions intercalated in the a-NTs is reinforced by the higher intensity of this transition compared to both the $CaCl_2$ aqueous solution and $CaCO_3$.

Finally, the amount of $Ca^{2+}$ trapped in the a-NTs can be estimated from the ratio of the edge jumps of the Ca and Ti K-edge XANES spectra. This gives a Ca/Ti ratio of 0.13, in very good agreement with the value of 0.11 eq. per $TiO_2$ formula unit obtained from the electrochemical signature.

## EXAFS Data Analysis

EXAFS data analysis was carried out to obtain a quantitative determination of the local structure around the $Ca^{2+}$ ion after its incorporation in the a-NT material. To this purpose, the theoretical SS signal of the oxygen nearest neighbors around the $Ca^{2+}$ centers was calculated and the structural parameters of the Ca–O distribution were optimized to obtain the best agreement with the experimental data. The results of the least-squares minimization performed in the $k$-range 3.2–10.0 Å$^{-1}$, shown in the upper panel of Figure 7, highlight a very good agreement between theoretical and experimental signals in both EXAFS and Fourier transform (FT) spectra. Note that the [1s3s] double-electron excitation was included in the model background function, while the multiplet corresponding to the [1s3s] transition falls outside the analyzed energy range.[20]

The optimized structural parameters for the Ca–O distribution are listed in Table 1, with $E_0 = 5.6$ eV above the first inflection point of the edge jump and $S_0^2 = 0.90$. These results show that the $Ca^{2+}$ ions are surrounded by an average number of 5.8(5) oxygens at a mean distance of 2.42(2) Å, very similar to the case of the $Ca^{2+}$ aqueous complex. This finding is not surprising given the similarity between the XANES spectrum of $Ca^{2+}$-intercalated a-NTs and that of the $CaCl_2$ aqueous solution (Figure 6b), and further corroborates the disordered environment around the incorporated $Ca^{2+}$ ions.

**Table 1.** Structural parameters for the Ca–O two-body distribution obtained from the EXAFS data analysis of the Ca K-edge absorption spectrum collected on a-NTs after full electrochemical $Ca^{2+}$ intercalation. $N$ is the coordination number, $R$ the average distance, $\sigma^2$ the Debye-Waller factor and $\beta$ the asymmetry index.

|  | $N$ | $R$ (Å) | $\sigma^2$ (Å$^2$) | $\beta$ |
|---|---|---|---|---|
| $Ca^{2+}$-intercalated a-NTs | 5.8(5) | 2.42(2) | 0.009(2) | 0.0(2) |

**Batteries & Supercaps**

Research Article
doi.org/10.1002/batt.202400183

**Chemistry Europe**
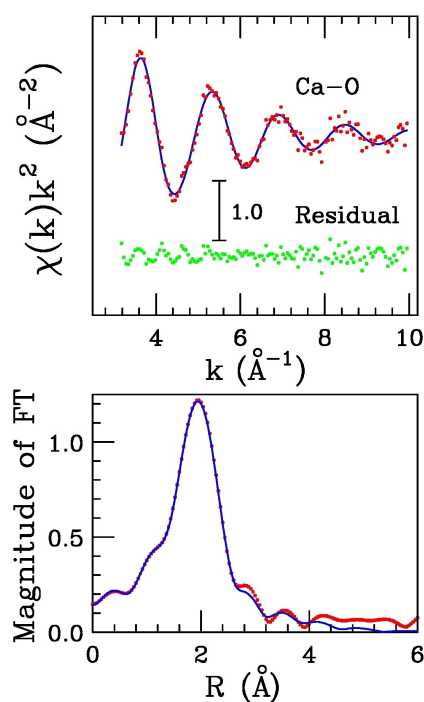European Chemical
Societies Publishing

**Figure 7.** Analysis of the Ca K-edge EXAFS spectrum collected on a-NTs after full electrochemical Ca$^{2+}$ intercalation. Upper panel: Ca–O theoretical signal (blue line) compared with the experimental data (red dots) and resulting residuals (green dots). Lower panel: non-phase shift corrected FTs of the best-fit EXAFS theoretical signal (blue line) and of the experimental data (red dots).

It is worth noting that, even though the EXAFS signal is dominated by the first shell oxygen contribution, the residual curve in Figure 6a shows the presence of an additional weak oscillation, most likely corresponding to Ti atoms sitting beyond the first-shell oxygen atoms. To verify this hypothesis, the EXAFS data analysis was carried out also by introducing the contribution of the second-shell Ti atoms with a SS Ca–Ti theoretical signal at an initial distance of 3.33 Å and a coordination number of 8.0, as taken in first approximation from the crystallographic structure of sodium titanate NaTi$_2$O$_4$.[65] The results of this fitting procedure are shown in Figure S2. As it can be observed, the inclusion of this additional contribution did not provide a significant improvement of the fit quality. Unfortunately, the Ca K-edge experimental XAS spectrum of this sample is quite noisy, and the available *k*-range is limited to 10.0 Å$^{-1}$. This hampers an adequate detection of the higher distance contributions and prevents the Ca–Ti structural parameters to be reliably extracted from the EXAFS data. For a similar reason, also the attempt to include a O–Ca–O MS contribution involving the first shell oxygen atoms resulted in a negligible improvement of the fit quality. To complement the XAS investigation, we carried out and XRD ex situ investigation of a-NT electrodes before and after calcium insertion (Figure S3). These diffractograms reveal a shift towards smaller angles for the peak at $2\theta = 48$, corresponding to an expansion of the (200) layer stacking upon calciation. This shift, observed between the pristine and *post mortem* samples, confirms the structural deformation observed by XAS.

## Conclusions

The electrochemical incorporation of Ca$^{2+}$ ions in the lattice of a-NTs synthesized via a hydrothermal route and preliminary characterized by FESEM-EDX, XRD, and Raman Spectroscopy was observed *vs.* both calcium metal and an activated carbon pseudocapacitive electrode using aprotic electrolytes. A-NTs are able to deliver a reversible (de)incorporation of 0.1-0.12 eq. of Ca$^{2+}$ ions at a working potential of 1.6 V *vs.* Ca$^{2+}$/Ca. This electrochemical activity is attributed to the reversible intercalation of the Ca$^{2+}$ ions, as demonstrated by *ex situ* Ca and Ti K-edge XAS analysis of a-NT sample after full discharge in a calcium metal half-cell. The intercalation induces a considerable amount of structural disorder around the Ti sites in the a-NT lattice, in between those observed upon lithiation and sodiation, in spite of the small amount of intercalated Ca$^{2+}$ cations. Nonetheless, the spectral profiles reveal that the typical fingerprint of anatase is maintained in the electrode material even after the intercalation. The analysis of the EXAFS data indicates that the incorporated Ca$^{2+}$ ions are surrounded by an average number of 5.8(5) oxygen neighbors at 2.42(2) Å. The emerging structural picture, in addition to providing clear evidence of the electrochemical intercalation of Ca$^{2+}$ in anatase, confirms that they are surrounded by a relatively disordered environment.

## Acknowledgements

## Conflict of Interests

The authors declare no conflict of interest.

## Data Availability Statement

The data that support the findings of this study are available from the corresponding author upon reasonable request.

[1] C. Deng, X. Li, R. Chen, K. Ye, J. Lipton, S. A. Maclean, H. Wang, A. D. Taylor, G. M. Weng, *Energy Storage Mater.* **2023**, *60*, https://doi.org/10.1016/j.ensm.2023.102820.

[2] L. Stievano, I. de Meatza, J. Bitenc, C. Cavallo, S. Brutti, M. A. Navarra, *J. Power Sources* **2021**, *482*, 228875, https://doi.org/10.1016/J.JPOWSOUR.2020.228875.

[3] L. Yan, W. Yang, H. Yu, L. Zhang, J. Shu, *Energy Storage Mater.* **2023**, *60*, https://doi.org/10.1016/j.ensm.2023.102822.

[4] J. D. Forero-Saboya, D. S. Tchitchekova, P. Johansson, M. R. Palacín, A. Ponrouch, *Adv. Mater. Interfaces* **2022**, *9* (8), https://doi.org/10.1002/admi.202101578.

[5] B. Ji, H. He, W. Yao, Y. Tang, *Adv. Mater.* **2021**, *33* (2), https://doi.org/10.1002/adma.202005501.

[6] S. Biria, S. Pathreeker, F. S. Genier, I. D. Hosein, A. Highly Conductive, *ACS Appl. Polym. Mater.* **2020**, *2* (6), 2111–2118, https://doi.org/10.1021/acsapm.9b01223.

[7] N. T. Hahn, D. M. Driscoll, Z. Yu, G. E. Sterbinsky, L. Cheng, M. Balasubramanian, K. R. Zavadil, *ACS Appl. Energ. Mater.* **2020**, *3* (9), 8437–8447, https://doi.org/10.1021/acsaem.0c01070.

[8] Z. Li, B. P. Vinayan, T. Diemant, R. J. Behm, M. Fichtner, Z. Zhao-Karger, *Small* **2020**, *16* (39), https://doi.org/10.1002/smll.202001806.

[9] N. T. Hahn, J. Self, D. M. Driscoll, N. Dandu, K. S. Han, V. Murugesan, K. T. Mueller, L. A. Curtiss, M. Balasubramanian, K. A. Persson, K. A. Persson, K. R. Zavadil, *Phys. Chem. Chem. Phys.* **2022**, *24* (2), 674–686, https://doi.org/10.1039/d1cp04370f.

[10] N. T. Hahn, S. A. McClary, A. T. Landers, K. R. Zavadil, *J. Phys. Chem. C* **2022**, *126* (25), 10335–10345, https://doi.org/10.1021/acs.jpcc.2c02587.

[11] H. R. Tinker, C. A. Howard, M. Zhou, Y. Xu, *Mater Adv* **2023**, *4* (9), 2028–2041, https://doi.org/10.1039/d2ma01034 h.

[12] S. Weng, G. Yang, S. Zhang, X. Liu, X. Zhang, Z. Liu, M. Cao, M. N. Ateş, Y. Li, L. Chen, Z. Wang, X. Wang, *Nano-Micro Lett.* **2023**, *15* (1), https://doi.org/10.1007/s40820-023-01183-6.

[13] Y. Tian, H. Yang, Y. Zeng, Y. Qi, W. Wang, H. Chen, W. Yin, Y. Ke, Z. Jian, W. H. Kan, W. H. Kan, W. Chen, *ACS Appl. Energ. Mater.* **2023**, *6* (7), 3854–3861, https://doi.org/10.1021/acsaem.2c04140.

[14] X. Zhao, H.-E. Wang, H. Chen, J. Cao, Y. Zhao, Z. Garbe Neale, W. Cai, J. Sui, G. Cao, *Energy Storage Mater.* **2018**, *11*, 161–169, https://doi.org/10.1016/j.ensm.2017.10.010.

[15] K. G. Reeves, J. Ma, M. Fukunishi, M. Salanne, S. Komaba, D. Dambournet, *ACS Appl Energy Mater* **2018**, *1* (5), 2078–2086, https://doi.org/10.1021/acsaem.8b00170.

[16] L. Duan, X. Li, *Synth. Met.* **2021**, *272*, https://doi.org/10.1016/j.synthmet.2020.116672.

[17] V. Gentili, S. Brutti, L. J. Hardwick, A. R. Armstrong, S. Panero, P. G. Bruce, *Chem. Mater.* **2012**, *24* (22), 4468–4476, https://doi.org/10.1021/cm302912f.

[18] D. L. Proffit, T. T. Fister, S. Kim, B. Pan, C. Liao, J. T. Vaughey, *J. Electrochem. Soc.* **2016**, *163* (13), A2508–A2514, https://doi.org/10.1149/2.0121613jes.

[19] U. Marini, B. Marconi, A. Petri, A. Di Cicco, M. J. Rosolen, R. Marassi, G. Aquilanti, M. Minicucci, E. Principi, N. Novello, A. Cognigni, L. Olivi, *J. Phys. Conf. Ser.* **2009**, *190* (1), 012043, https://doi.org/10.1088/1742-6596/190/1/012043.

[20] P. D'Angelo, P. E. Petit, N. V. Pavel, *J. Phys. Chem. B* **2004**, *108* (31), 11857–11865, https://doi.org/10.1021/JP048511L.

[21] A. Filipponi, A. Di Cicco, *Phys. Rev. B* **1995**, *52* (21), 15122–15134, https://doi.org/10.1103/PhysRevB.52.15122.

[22] A. Filipponi, A. Di Cicco, *Phys. Rev. B* **1995**, *52* (21), 15135–15149, https://doi.org/10.1103/PhysRevB.52.15135.

[23] L. Hedin, S. Lundqvist, *Solid State Phys. – Advances in Research and Applications* **1970**, *23* (C), 1–181, https://doi.org/10.1016/S0081-1947(08)60615-3.

[24] M. Busato, A. Melchior, V. Migliorati, A. Colella, I. Persson, G. Mancini, D. Veclani, P. D'Angelo, *Inorg. Chem.* **2020**, *59* (23), 17291–17302, https://doi.org/10.1021/ACS.INORGCHEM.0C02494.

[25] J. A. van Bokhoven, C. Lamberti, *X-Ray Absorption and X-Ray Emission Spectroscopy: Theory and Applications* **2015**, *1–2*, 1–845, https://doi.org/10.1002/9781118844243.

[26] T. Ohsaka, F. Izumi, Y. Fujiki, *J. Raman Spectrosc.* **1978**, *7* (6), 321–324, https://doi.org/10.1002/JRS.1250070606.

[27] T. Beuvier, M. Richard-Plouet, L. Brohan, *J. Phys. Chem. C* **2009**, *113* (31), 13703–13706, https://doi.org/10.1021/JP903755P.

[28] M. Salari, K. Konstantinov, H. K. Liu, *J. Mater. Chem.* **2011**, *21* (13), 5128–5133https://doi.org/10.1039/c0jm04085a.

[29] A. Rendón-Rivera, J. A. Toledo-Antonio, M. A. Cortés-Jácome, C. Angeles-Chávez, *Catal. Today* **2011**, *166*, 18–24, https://doi.org/10.1016/j.cattod.2010.03.045.

[30] A. Tamilselvan, S. Balakumar, *Ionics (Kiel)* **2016**, *22* (1), 99–105, https://doi.org/10.1007/S11581-015-1526-8/METRICS.

[31] L. J. Hardwick, M. Holzapfel, P. Novák, L. Dupont, E. Baudrin, *Electrochim. Acta* **2007**, *52* (17), 5357–5367, https://doi.org/10.1016/J.ELECTACTA.2007.02.050.

[32] G. S. Zakharova, *Russ. J. Inorg. Chem.* **2014**, *59* (2), 24–28, https://doi.org/10.1134/S0036023614020235.

[33] I. R. Beattie, T. R. Gilson, *Proc R Soc Lond A Math Phys Sci* **1968**, *307* (1491), 407–429, https://doi.org/10.1098/RSPA.1968.0199.

[34] M. Hodos, H. Haspel, E. Horváth, Á. Kukovecz, Z. Kónya, I. Kiricsi, *AIP Conf. Proc.* **2005**, *786*, 345–348, https://doi.org/10.1063/1.2103884.

[35] V. Gentili, S. Brutti, L. J. Hardwick, A. R. Armstrong, S. Panero, P. G. Bruce, *Chem. Mater.* **2012**, *24* (22), 4468–4476, https://doi.org/10.1021/CM302912F.

[36] S. A. Hamdan, I. M. Ibrahim, I. M. Ali, *Dig. J. Nanomater. Biostruct.* **2020**, *15* (4), 1001–1008, https://doi.org/10.15251/djnb.2020.154.1001.

[37] E. V. Salomatina, A. S. Loginova, S. Ignatov, A. V. Knyazev, I. V. Spirina, L. A. Smirnova, *J. Inorg. Organomet. Polym. Mater.* **2016**, *26* (6), 1280–1291, https://doi.org/10.1007/S10904-016-0409-4.

[38] S. W. Oh, S. H. Park, Y. K. Sun, *J. Power Sources* **2006**, *161* (2), 1314–1318, https://doi.org/10.1016/J.JPOWSOUR.2006.05.050.

[39] J. Forero-Saboya, C. Davoisne, R. Dedryvère, I. Yousef, P. Canepa, A. Ponrouch, *Energy Environ. Sci.* **2020**, *13* (10), 3423–3431, https://doi.org/10.1039/d0ee02347g.

[40] D. Wang, X. Gao, Y. Chen, L. Jin, C. Kuss, P. G. Bruce, *Nat. Mater.* **2018**, *17*, 16–20, https://doi.org/10.1038/nmat5036.

[41] A. Shyamsunder, L. E. Blanc, A. Assoud, L. F. Nazar, *ACS Energy Lett.* **2019**, *4* (9), 2271–2276, https://doi.org/10.1021/ACSENERGYLETT.9B01550.

[42] X. Liu, G. A. Elia, S. Passerini, *J. Power Sources Adv.* **2020**, *2*, https://doi.org/10.1016/J.POWERA.2020.100008.

[43] Z. Li, O. Fuhr, M. Fichtner, *Energy Environ. Sci.* **2019**, *12* (12), 3496–3501, https://doi.org/10.1039/C9EE01699F.

[44] Z. Yang, D. Choi, S. Kerisit, K. M. Rosso, D. Wang, J. Zhang, G. Graff, J. Liu, *J. Power Sources* **2009**, *192* (2), 588–598, https://doi.org/10.1016/J.JPOWSOUR.2009.02.038.

[45] Q. Wei, X. Chang, D. Butts, R. DeBlock, K. Lan, J. Li, D. Chao, D. L. Peng, B. Dunn, *Nat. Commun.* **2023**, *14* (1), 1–9, https://doi.org/10.1038/s41467-022-35617-3.

[46] T. C. Rossi, D. Grolimund, M. Nachtegaal, O. Cannelli, G. F. Mancini, C. Bacellar, D. Kinschel, J. R. Rouxel, N. Ohannessian, D. Pergolesi, T. Lippert, M. Chergui, *Phys. Rev. B* **2019**, *10* (24), 245207, https://doi.org/10.1103/PHYSREVB.100.245207.

[47] V. Luca, *J. Phys. Chem. C* **2009**, *113* (16), 6367–6380, https://doi.org/10.1021/JP808358V.

[48] P. C. Angelomé, L. Andrini, M. E. Calvo, F. G. Requejo, S. A. Bilmes, G. J. A. A. Soler-Illia, *J. Phys. Chem. C* **2007**, *111* (29), 10886–10893, https://doi.org/10.1021/JP069020Z.

[49] T. Yamamoto, *X-Ray Spectrum.* **2008**, *37* (6), 572–584, https://doi.org/10.1002/XRS.1103.

[50] D. Cabaret, A. Bordage, A. Juhin, M. Arfaoui, E. Gaudry, *Phys. Chem. Chem. Phys.* **2010**, *12* (21), 5619–5633, https://doi.org/10.1039/B926499J.

[51] K. Schneider, D. Zajac, M. Sikora, C. Kapusta, K. Michalow-Mauke, T. Graule, M. Rekas, *Radiat. Phys. Chem.* **2015**, *112*, 195–198, https://doi.org/10.1016/J.RADPHYSCHEM.2015.03.010.

[52] Y. Joly, D. Cabaret, H. Renevier, C. R. Natoli, *Phys. Rev. Lett.* **1999**, *82* (11), 2398, https://doi.org/10.1103/PhysRevLett.82.2398.

[53] F. Farges, G. E. Brown, *Phys. Rev. B* **1997**, *56* (4), 1809, https://doi.org/10.1103/PhysRevB.56.1809.

**Batteries & Supercaps**

Research Article
**doi.org/10.1002/batt.202400183**

**Chemistry Europe**
European Chemical
Societies Publishing

[54] G. Greco, K. A. Mazzio, X. Dou, E. Gericke, R. Wendt, M. Krumrey, S. Passerini, *ACS Appl. Energ. Mater.* **2019**, *2* (10), 7142–7151, https://doi.org/10.1021/ACSAEM.9B01101.

[55] A. Siebert, X. Dou, R. Garcia-Diez, D. Buchholz, R. Félix, E. Handick, G. Greco, I. Hasa, R. G. Wilks, S. Passerini, M. Bär, *ACS Appl. Energ. Mater.* **2021**, *4* (1), 164–175, https://doi.org/10.1021/ACSAEM.0C02025.

[56] D. Wang, L. Liu, X. Sun, T. K. Sham, *J. Mater. Chem. A* **2014**, *3* (1), 412–419, https://doi.org/10.1039/C4TA04873C.

[57] M. Fehse, L. Monconduit, F. Fischer, C. Tessier, L. Stievano, *Solid State Ionics* **2014**, *268 (PB)*, 252–255, https://doi.org/10.1016/J.SSI.2014.09.018.

[58] U. Lafont, D. Carta, G. Mountjoy, A. V. Chadwick, E. M. Kelder, *J. Phys. Chem. C* **2010**, *114* (2), 1372–1378, https://doi.org/10.1021/JP908786T.

[59] V. Luca, T. L. Hanley, N. K. Roberts, R. F. Howe, *Chem. Informationsdienst* **1999**, *30* (43), no-no, https://doi.org/10.1002/CHIN.199943012.

[60] J. Ma, W. Li, B. J. Morgan, J. Światowska, R. Baddour-Hadjean, M. Body, C. Legein, O. J. Borkiewicz, S. Leclerc, H. Groult, F. Lantelme, C. Laberty-Robert, D. Dambournet, *Chem. Mater.* **2018**, *30* (9), 3078–3089, https://doi.org/10.1021/acs.chemmater.8b00925.

[61] J. Li, J. Liu, Q. Sun, M. N. Banis, X. Sun, T. K. Sham, *J. Phys. Chem. C* **2017**, *121* (21), 11773–11782, https://doi.org/10.1021/ACS.JPCC.7B01106.

[62] W. Li, M. Fukunishi, B. J. Morgan, O. J. Borkiewicz, K. W. Chapman, V. Pralong, A. Maignan, O. I. Lebedev, J. Ma, H. Groult, S. Komaba, D. Dambournet, *Chem. Mater.* **2017**, *29* (4), 1836–1844, https://doi.org/10.1021/acs.chemmater.7b00098.

[63] R. D. Shannon, *Acta Crystallogr.* **1976**, *A32*, 751–767, Acta Crystallogr. 1976, A32, 751–767 .

[64] F. Jalilehvand, D. Spångberg, P. Lindqvist-Reis, K. Hermansson, I. Persson, M. Sandström, *J. Am. Chem. Soc.* **2001**, *123* (3), 431–441, https://doi.org/10.1021/JA001533A .

[65] J. Akimoto, H. Takei, *J. Solid State Chem.* **1989**, *79* (2), 212–217, https://doi.org/10.1016/0022-4596(89)90268-5.